Atomistic simulation of the mechanical properties of nanoporous gold

J.F. Rodriguez-Nieva [a,1], C.J. Ruestes [b,c], Y. Tang [d], E.M. Bringa [b,c,*]

[a] *Instituto Balseiro, Universidad Nacional de Cuyo, 8400 Bariloche, Argentina*
[b] *Facultad de Ciencias Exactas y Naturales, Universidad Nacional de Cuyo, 5500 Mendoza, Argentina*
[c] *CONICET, Mendoza 5500, Argentina*
[d] *Shanghai Institute of Applied Mathematics and Mechanics, Shanghai University, Shanghai 200072, China*

Abstract

We study the mechanical behavior of nanoporous gold under uniaxial compression and strain rates in the range of 10^7–10^9 s^{-1} using molecular dynamics simulations. We consider the low-porosity regime (porosity of $\sim$5%), which is characterized by several stages of plastic deformation. At the onset of plasticity, pores act as if isolated by emitting "shear" dislocation loops. At higher deformations, the mechanical response is determined by the interactions between dislocations in the dense dislocation forest, leading to strain hardening. Increasing the strain rate results in an increasing flow stress ranging from 0.4 to 0.7 GPa within the range of applied strain rates. The von Mises stress σ_{VM} in the hardening regime features two possible power-law dependencies as a function of dislocation density ρ_d: in the initial stages of plastic deformation we obtained $\sigma_{VM} \propto \rho_d^2$, but changes to Taylor hardening $\sigma_{VM} \propto \rho_d^{1/2}$ at higher dislocation densities. The velocity of dislocations is estimated to be $\sim$60% of the speed of sound in the early stages of plastic deformation, but later decreases dramatically due to dislocation–dislocation and dislocation–pore interactions. The unloading of the complex dislocation and stacking fault network leads to the production of vacancies. As a result, we propose that the vacancy clusters observed experimentally in recovered samples and attributed to "dislocation-free" plasticity are instead due to the aggregation of those vacancies left behind during recovery.
© 2014 Acta Materialia Inc. Published by Elsevier Ltd. All rights reserved.

1. Introduction

The mechanical behavior of nanomaterials can be significantly superior to the behavior of conventional materials in several important ways. For instance, the reduction of the grain size in polycrystals results both in ultrastrong materials [1,2] and increased radiation resistance [3]. Alternatively, the addition of nanoscale defects such as nanotwins [4] can substantially increase ductility without affecting strength. Nanoporous materials [5] are a different class of nanostructured materials which feature a large variety of

properties that can be exploited in different fields of science and engineering. Their reduced weight but enhanced strength and ductility are of great interest in aerospace and automotive applications, while their high surface-to-volume ratio makes them ideal for catalysis or energy storage [6]. Additionally, the radiation resistance of nanofoams can potentially be enhanced because nanopores may act as efficient sinks for radiation-induced defects [7]. New pathways to design more efficient nuclear fuels may be implemented with nanopores, considering that conventional fuels typically become open-cell foams with relative densities of 70% due to the insolubility of fission gases in the matrix.

Most of the current experiments studying mechanical properties of metallic nanofoams involve nanoindentation and quasistatic deformation [5,8,9]. However, some

---

* Corresponding author at: Facultad de Ciencias Exactas y Naturales, Universidad Nacional de Cuyo, 5500 Mendoza, Argentina.
  E-mail address: ebringa@yahoo.com (E.M. Bringa).
[1] Current address: Massachusetts Institute of Technology, Cambridge, MA 02139, USA.

potential applications, such as impact shields, require understanding the behavior at high strain rates. Such experiments typically include in situ diagnostics limited to wave velocity or stress profiles, showing delays related to pore collapse [10,11]. The increasing availability of high-intensity, ultrafast X-ray sources opens the possibility for novel studies by looking at in situ plastic deformation [12–14], but we are not aware of such experiments in nanoporous materials to date. We also note that porosity makes the preparation of pre- or post-loaded (recovered) samples for electron microscopy very challenging.

The role of continuum and atomistic simulations is crucial both to help understand and plan future experiments and to access regimes that are currently inaccessible experimentally. The validity of continuum models that include porosity [15,16] at the nanoscale is, however, not yet clear. In Gurson's original model [15], the yield criteria is void-size independent and is only a function of porosity. This is in disagreement with more detailed atomistic simulations of void growth in both face-centered cubic (fcc) [17,18] and body-centered cubic (bcc) [19] metals, which showed that yielding in the nanoscale regime strongly depends on void size. The modified Gurson model [16] incorporates a Taylor dislocation model to account for the void-size effect on yielding, but its validity still needs to be examined for nanoporosity.

Atomistic simulations play a twofold role. Not only can they provide unique insights of the processes occurring at the nanoscale, but they can also help produce new constitutive models valid at the microscale for large length-scale simulations, as demonstrated in Ref. [17]. In particular, molecular dynamics (MD) simulations allow study of the time-evolution of a large number of atoms using empirical potentials in order to obtain detailed information about deformation, stress, temperature, etc. Consequently, MD simulations are ideal for the study of nanoscale defects such as nanopores.

Relatively few studies of nanoporous materials using MD are available. Erhart et al. [11] studied the compression of nanoporous Cu and Al, with porosities of up to 20%. Nanoporous foams with porosities larger than 50% (similar to the ones obtained by dealloying) have been studied by Crowson et al. [20,21], Gyulassi et al. [22], and Kolluri and Demkowikcz [23]. Other recent simulations of high-porosity gold nanofoams also find several remarkable features, such as expansion under tension [24]. Studies of void interactions and coalescence of nanoporous silica glass under hydrostatic tension were performed by Chen et al. [25]. Additionally, the deformation and growth of voids has been studied in several papers [17–19,26], yet it is still debated whether such growth is due to dislocation nucleation [26].

In the present work we study the mechanical behavior of nanoporous gold under high strain rates and uniaxial compression, and builds on previous work on plastic deformation induced by a single void in fcc materials [27,28] and a recent brief study for nanoporous bcc tantalum [29]. Here, we consider a regime characterized by relatively small porosity ($\sim$5%) so that pores and their interactions mainly determine the mechanical response. Such low porosities are found in samples with radiation damage [10] or in the early stages of plastic failure, as in samples with pre-spall [11]. Our regime is different from previous high-porosity simulations [20–23] in which the mechanical response is qualitatively described as the collapse or fracture of nanopillars in a reticular type of structure, as described below.

The outline of the paper is as follows: in Section 2, we provide a general qualitative description of the different regimes of the mechanical response of a nanoporous solid. In Section 3, we describe the details of the MD simulation. In Section 4, we present the results of the simulations, and discuss the activation mechanism of plastic deformation, dislocation dynamics, strain-rate effects, and comparison with experimental results. In Section 5 we present a summary of the results and the conclusions.

2. Porosity regimes in the mechanical behavior of nanoporous materials

A nanoporous material can be qualitatively described by its mean pore radius r and the mean inter-pore distance d. It is important to note that the mechanical response will be intrinsically different depending on the level of porosity, or more quantitatively, on d/r. We identify four possible scenarios for the mechanical response:

(i) Perfect crystal ($r \to 0$): in this case there are no favorable points for the production of dislocations, which are produced by homogeneous nucleation [30].

(ii) Isolated pores ($d/r \gg 10$): this regime was studied for different systems, both for traction as well as compression [27,31–33]. In Ref. [28] it was found that vacancy clusters with up to $\sim$10 vacancies behave similarly to the perfect crystal case at high strain rates. For a larger pore size, the flow stress decreases as $\sigma_Y \propto r^{-1}$ at the nanoscale, reaching a nearly constant value for microscopic radii.

(iii) Interacting pores ($2 < d/r < 10$): in this regime, the initiation of plastic deformation occurs similarly to the isolated pore case, but with a slightly lowered yield stress due to the long-range stress field of the pores. The important difference with regime (ii) is that dislocations from one pore interact strongly with the dislocations from other pores when they travel a distance equal to $\sim (d/2 - r)$, leading to a second stage of plastic deformation which is characterized by dislocation reactions and formation of dislocation junctions.

(iv) Low-density materials (nanofoams, $d/r \approx 2$): in this case, the filaments behave as nanopilars and the dislocation nucleation and evolution is heavily dependent on their size and structure [34]. There are many simulations of nanopillars [5,34,35], but the mechanical behavior of nanofoams will be greatly influenced by nanopilar junctions and possible pre-existing defects [24], especially if there are grains which can lead to grain-boundary sliding.

These scenarios would apply to nanoporous solids independently of atomic structure details. In this work, we focus on scenario (iii) for an fcc crystal, which although sharing some qualitative features with the mechanical response of a bcc crystal [29], differs significantly in the resulting microstructure, as discussed in the following sections. We also explore other aspects of the dislocation activity, including mobile dislocation estimates.

3. Simulation details

We consider a cubic gold single crystal (fcc structure with lattice parameter $a_0 = 0.408$ nm) containing spherical pores of radius 10 a_0. The pores are distributed randomly without superposition, as shown in Fig. 1. The sample used was of size $100a_0 \times 100a_0 \times 100a_0$, with 10 pores and a total of 3.8 million atoms. The minimum void-to-void distance is $d_{\min} = 11.8$ nm (filament of size 3.6 nm), while the average distance is $d \sim 17.7$ nm. We used the embedded atom method (EAM) potential for Au [36,37], which has been already used for simulations of nanofoams [21,23]. The initial temperature of the sample was of 10 K, with periodic boundary conditions in every direction to model an infinite solid. The low initial temperature is chosen to simplify defect detection, but simulations at room temperature show the same features.

Uniaxial strain deformation was applied in the [001] direction, leaving all other directions without deformation. We used a wide range of strain rates, from 10^7 to 10^9 s^{-1}. These strain rates and strain modes are representative of shock experiments [38], where strain in the direction perpendicular to loading can be neglected during the early stages of deformation.

In the following, we quantify shear stress using the von Mises stress, defined as:

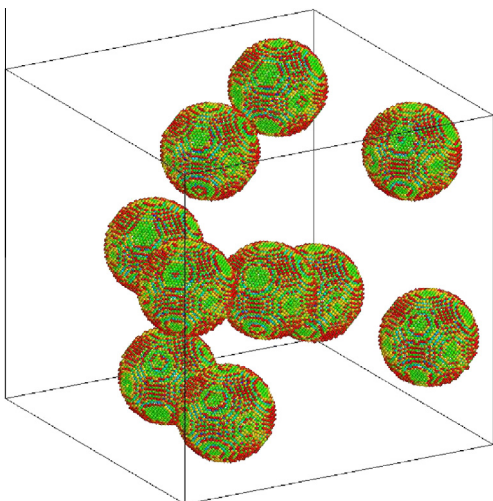$$\sigma_{\mathrm{VM}} = \sqrt{\frac{3}{2} s_{ij} s_{ij}}, \quad s_{ij} = \sigma_{ij} - \sigma_{kk} \delta_{ij}/3, \tag{1}$$

where the stress tensor σ_{ij} is obtained from the MD simulations.

4. Results

4.1. Activation mechanism for plastic deformation

Useful insights about the mechanical response of nanofoams can be obtained if the evolution of a system with an isolated pore is compared with the evolution of a system with multiple pores. We consider the response of each case at a strain rate of 10^9 s^{-1} in the [001] direction. The stress–strain curves are plotted in Fig. 2(a), where the case of a defect-free crystal is also included for comparison. In the perfect crystal case, there is no emission of dislocations from pre-existing defects. Adding a void into the sample results in the material yielding due to dislocation emission from that void. If the number of dislocation sources (voids) is increased, the material can yield at an even lower stress.

Nucleation occurs at a strain of 2.5% and a von Mises stress of 0.6 and 0.5 GPa for the single void and 10 void sample, respectively, as shown in Fig. 2(a). The similar yield strain between both cases is an indication that pores behave almost independently when plastic deformation begins. The stress level required for dislocation nucleation in gold is lower than for bcc crystals (3–4 GPa for Ta [29]) due to the much higher lattice resistance of the bcc structure (higher shear modulus, higher generalized stacking fault energies).

The Gibson–Ashby formalism for yielding in open-cell foams can be used for low-density nanoporous Au by considering a size-dependent strength of the nanopillars in the foam [24,39]. In our case, such formalism is not valid given the high density (small porosity) of the sample.

Fig. 1. Nanoporous sample used in the simulations. Only atoms located at the surface of the pores are visible.
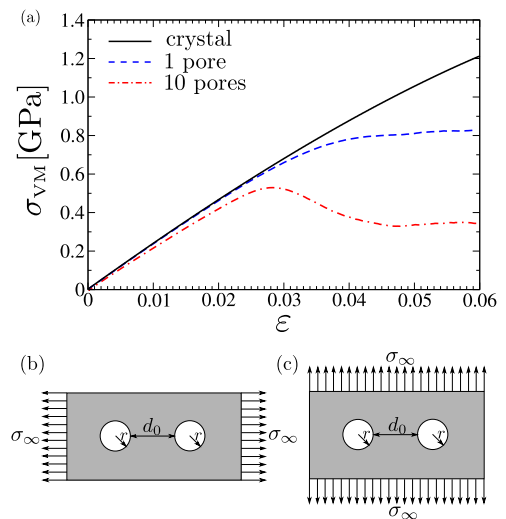

Fig. 2. (a) Stress–strain curves for three samples with: no pores, a single pore and 10 pores. Geometry of the 2-D Wu–Markenscoff model for the stress amplification due to two holes of equal radius r and separated by a distance d_0, and under a stress field σ_∞ (b) parallel or (c) perpendicular to the intervoid direction.

Alternatively, an estimation of the singular stress amplification due to two neighboring voids can be calculated with the aid of the Wu–Markenscoff model [40]. This 2-D model considers the singular stress amplification between two holes of equal radius and, despite being a 2-D analysis, it allows a first-order estimate of the stress amplification. The simplest formulation for uniaxial loading considering two neighboring holes yields a maximum stress amplification:

$$\sigma_{\max} \approx \left[\frac{1.94}{\sqrt{d_0/2r}} \mp \frac{\sqrt{2}}{2\sqrt{d_0/2r}} \right] \sigma_{\infty}, \qquad (2)$$

where σ_{∞} is the stress at an infinite distance from the holes, r is the hole radius, and $d_0 = d - 2r$ is the distance between the edges of the holes. The minus sign corresponds to the hole centers aligned with the axis of loading (Fig. 2(b)) and the plus sign corresponds to the perpendicular alignment (Fig. 2(c)). Here, we set $d_0 \sim 10.0$ nm and $r \sim 4.0$ nm, and obtain $\sigma_{\max} \sim 1.1\sigma_{\infty}$ for longitudinal tension and $\sigma_{\max} \sim 2.4\sigma_{\infty}$ for transverse tension. In the case of a set of voids randomly distributed within the sample, we can assume that the amplification falls in between. The ratio between the (remote) dislocation nucleating stresses for the single void σ_{1v} and the 10 void configuration σ_{10v} obtained from the MD simulations (Fig. 2) is given by

$$\frac{\sigma_{1v}}{\sigma_{10v}} = \frac{0.6\ \mathrm{GPa}}{0.5\ \mathrm{GPa}} \sim 1.2, \qquad (3)$$

and is consistent with the Wu–Markenscoff model. Thus, the relatively small distance between voids amplifies the local stress and decreases the far-field stress required for dislocation loop emission.

4.2. Dislocation evolution

In order to quantify plastic activity, we applied the centrosymmetry parameter (csp) [41] filter to obtain the dislocation densities. We first extract the atoms from partial dislocations using filter values of $4.0 < csp < 6.5$. The dislocation density was then calculated as in previous work [13,42]

$$\rho_d = Ns/(AV), \qquad (4)$$

where N is the number of atoms in the dislocations according to the csp filter, s is the distance between those atoms ($s \sim a_0$) and V is the volume of the sample. The parameter A takes into account how many atoms are in the dislocation core according to the filter used [42]. Since the csp gives two planes of atoms for a single partial dislocation, then $A = 2$. The dislocation densities for the samples with 1 and 10 voids are shown in Fig. 3. Initially, the sample with 10 voids has a dislocation density an order of magnitude higher than the single void sample. This serves as an additional confirmation that voids behave independently at the initiation of plastic deformation. At higher strains, however, this difference is no longer observed due to the
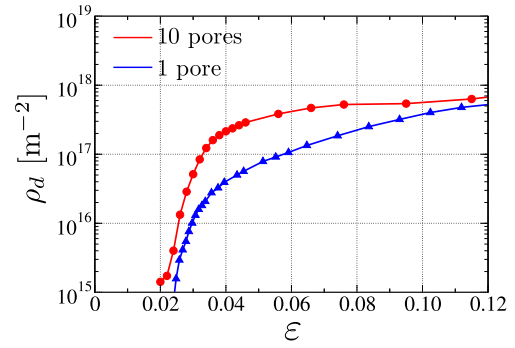

Fig. 3. The dislocation density ρ_d as a function of strain ε for a sample with a single pore, and a sample with 10 pores.

fact that the simulation box is completely filled with dislocations accommodating the same external strain.

The evolution of dislocations is shown in Figs. 4 and 5 for an isolated pore and for multiple random pores, respectively. In the single-pore sample, dislocations are able to move independently for longer times due to the lack of obstacles. In the sample with multiple voids, dislocations evolve in a similar fashion at the beginning of plastic deformation, but quickly start to interact with other dislocations and pores.

Dislocation emission from individual voids happens as described in detail for fcc Cu [13,17,43]: incomplete shear
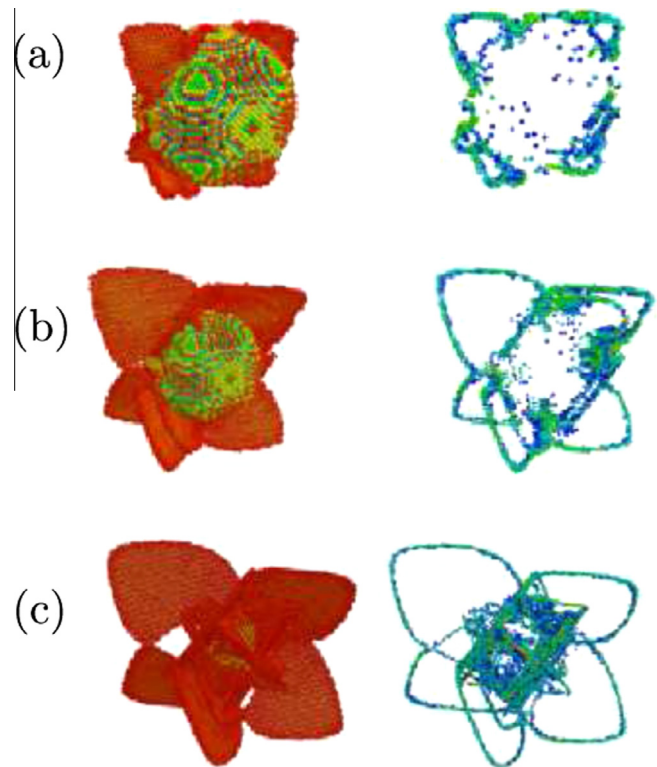

Fig. 4. Creation of dislocations from a single pore of radius 4 nm in a gold crystal: (a) $\varepsilon = 2.5\%$, (b) $\varepsilon = 2.8\%$, (c) $\varepsilon = 3.3\%$ for two different ranges of the centrosymmetry parameter (csp), to show stacking faults and surfaces (left column), or partial dislocations (right column).
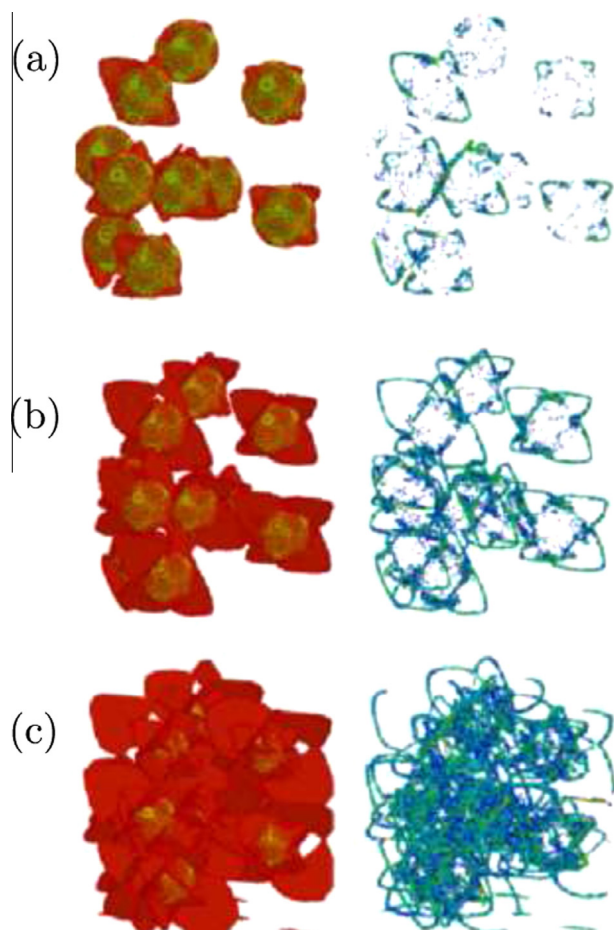
Fig. 5. Creation of dislocations from multiple 4 nm pores: (a) $\varepsilon = 2.5\%$, (b) $\varepsilon = 2.8\%$, (c) $\varepsilon = 3.3\%$ for two different ranges of csp, to show stacking faults and surfaces (left column), or partial dislocations (right column). Before the dislocations begin to interact, the behavior is qualitatively similar to that of Fig. 4.

[17,47], and less than 1% are perfect fcc dislocations (with a SF ribbon separating two partial dislocations). The remaining $\sim 9\%$ of dislocations could not be identified as standard fcc dislocations likely due to immense local strains which makes a Burgers circuit construction difficult. Fig. 6 shows a snapshot analyzed with DXA. In agreement with previous studies for a single void in fcc metals [17,47], prismatic loop formation is not observed [44,45].

Due to the low SF energy of Au, samples might readily twin [48,49]. We do not observe twinning in our simulations, but it might occur at longer times or for dislocation sources different from the voids used here.

Plastic activity leads to pore collapse in relatively short time scales, indicating qualitatively similar behavior to what has been shown for Cu crystals [17]. In our simulations for a strain rate of $10^9 \, \text{s}^{-1}$, void volume has been reduced by 80% at 6% strain, with total void closure by 7% strain. Pore collapse can be related to the density of geometrically necessary dislocations (GNDs) needed to transport vacancies away from the voids. Using the same model as Traiviratana et al. [17], we can assume an extension of the plastic regions around the voids equal to half the distance among voids, $d/2$, and use $k = d/2r = 8.8/4.0 = 2.2$, where k is the extension ratio of the loop from its original value. This gives a GND density of $3.5 \times 10^{16}/\text{m}^2$. The strain at which the plastic zones extend nearly halfway towards neighboring voids occurs at 3% (Fig. 5 snapshots). At this point, the dislocation densities are $\sim 10^{17}/\text{m}^2$, which is somewhat larger than the analytical estimate above. Therefore, the dislocation density we find is sufficient to cause pore collapse without contributions from diffusive processes.

loops, consisting of partial dislocations ahead of stacking faults (SFs), are emitted on all four {1 1 1} planes, and remain attached to the void surfaces in order to allow the voids to collapse [44,45]. At large strains, the box contains a forest of partial dislocations, together with few full dislocations (leading and trailing partial dislocations with a stacking fault between them). This is in contrast with bcc nanoporous solids, where there are neither partial dislocations nor stacking faults, but a forest consisting mostly of screw dislocations [29].

We applied the Dislocation eXtraction Algorithm (DXA) [46] to the sample with 10 voids at different strains. The DXA analysis on the nucleated dislocations at 2.5% strain reveals that all of them are Shockley partials, with their Burgers vectors as expected for fcc materials [17]. These partials are typically leading partials bounding an intrinsic stacking fault, with stacking sequence ABCA-CABC, in all available {1 1 1} planes. The DXA analysis on the dislocations at 3.3% strain reveals multiple dislocation junctions: 77% of dislocations are Shockley partials, 13% are stair-rod dislocations due to dislocation junctions
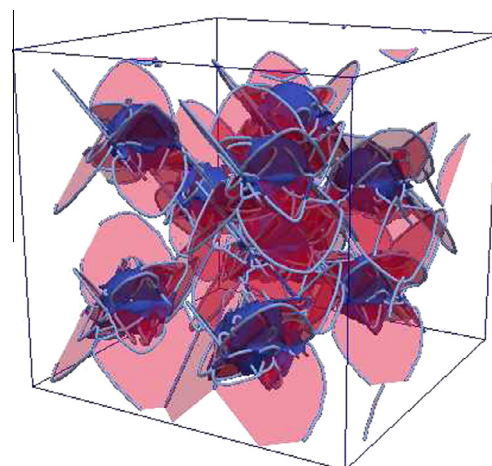

Fig. 6. The Dislocation eXtraction Algorithm (DXA) [46] analysis on the dislocations at 3.3% strain for the sample with 10 pores reveals that most dislocations are partials (thick blue lines), bounding intrinsic stacking faults (translucent pink surfaces). Void surfaces are indicated in blue. (For interpretation of the references to colour in this figure legend, the reader is referred to the web version of this article.)

4.3. Velocity of dislocations

Several studies have focused on dislocation dynamics in copper [50,51], aluminium, nickel and Al–Mg alloys [52] as well as dislocation drag and inertia in nickel [53,54]. The behavior of dislocations with shear stress is complex and we do not intend to reproduce these detailed studies on dislocation velocities. However, using our results we can determine the dislocation speed v_d in Au as a function of stress as:

$$v_d = \frac{d}{2\Delta\varepsilon}\frac{d\varepsilon}{dt}, \tag{5}$$

where $\Delta\varepsilon = \varepsilon_{hard} - \varepsilon_{pl}$, with ε_{pl} is the strain where plastic deformation begins and ε_{hard} is the deformation at which hardening begins. For $\Delta\varepsilon$, we use values at different strain rates and we take an average stress in the plateau of plastic deformation (see Fig. 9 below). The velocity v_d of the dislocations as a function of the von Mises stress is plotted in Fig. 7, and shows a velocity approximately linear with tension as is usually assumed in the viscous phonon drag regime [52], where $v_d = (b/B)\sigma$, and B is the drag coefficient. We obtain $B \sim 1.5 \times 10^{-4}$ Pa s, which has similar values to the ones obtained in simulations of other fcc metals [50,52]. These velocities calculated above are effective velocities for the whole sample.

Alternatively, by tracking the coordinates of the dislocations in the simulations, we can also obtain dislocation velocities. We observe an initial velocity of ~ 2 km s^{-1}, which is close to the Rayleigh speed in Au and near the maximum velocity for subsonic dislocations. In this case, the leading partial dislocations would move faster than a full dislocation where the trailing partial would provide additional drag forces. After a short time, dislocation velocities decrease about one order of magnitude given that they form a network with multiple sessile junctions. Plastic heating increases the temperature of the sample by $\sim$100 K. This is enough to increase dislocation mobility [54], but would not modify greatly the nucleation stress of dislocations from surfaces of voids [55].

4.4. Mobile dislocation density

The amount of plastic work is an important quantity to be evaluated in our nanoporous sample. The kinematic relationship between the plastic strain rate (in terms of the mobile dislocation density ρ_M) and the mean distance traveled by a dislocation is given by [56]

$$\dot{\varepsilon} = bv\rho_M, \tag{6}$$

where b is the Burgers vector ($b = a/2\sqrt{2} = 0.288$ nm at room conditions, a being the Au lattice constant) and v is the average dislocation velocity.

Recently, Higginbotham et al. [57] found that plastic heating can be described accurately by simple equations even at very high strain rates, provided the stress and temperature history are known. Based on Ref. [57], the temperature rise dT associated with plastic deformation is:

$$dT = \frac{\beta}{C}\sigma\,d\varepsilon, \tag{7}$$

where C is the heat capacity, $\sigma(t)$ is the time-dependent shear stress, and β is an empirical parameter that represents the fraction of rate of plastic work dissipated as heat [58]. Taking the time derivative of Eq. (7) and inserting into Eq. (6), we then obtain:

$$\rho_M = \frac{C\rho}{\sigma(t)\beta b\bar{v}}\frac{dT}{dt}. \tag{8}$$

Eq. (8) can also be derived [57] for a material with a well-defined compliance, and with a single dislocation dipole subjected to rapid shear strain. The results of Higginbotham et al. were obtained for a set of conditions not entirely met in our study, and therefore we emphasize that the methodology as applied here only provides a rough approximation for the mobile dislocations.

Fig. 8 shows the mobile dislocation density results, using an average dislocation velocity of 2 km s^{-1}. As expected from the snapshots in Fig. 5, the total density and the mobile density are close to each other at the initiation of plastic activity. However, the rapid formation of junctions leads to a decrease in mobile dislocations with respect to the total number of dislocations, with a difference of over
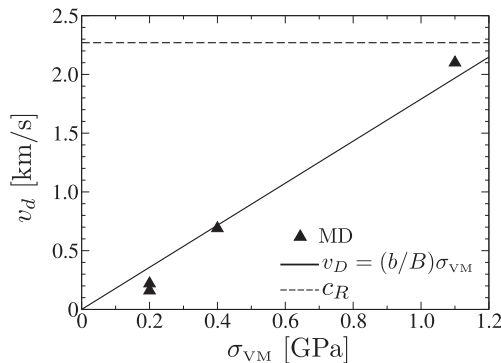

Fig. 7. Velocity of the dislocations as a function of the von Mises stress for the sample with 10 voids. Here, b denotes Burgers vector, c_R is the Rayleigh velocity, and B is the drag coefficient [50,52].
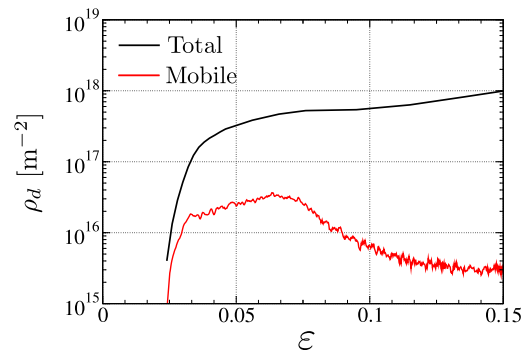

Fig. 8. Mobile and total dislocation densities as a function of strain, using the model of Higginbotham [57].

one order of magnitude at large strains. This is also consistent with previous results [13,42], which showed that mobile dislocations are diminished once large dislocation densities are produced by homogeneous nucleation, resulting in the formation of dislocation junctions.

4.5. Strain-rate effects and the hardening regime

Using non-equilibrium atomistic simulations, we are limited to high-strain-rate behavior. As shown in Fig. 9, increasing the strain rate results in a higher yield strain and yield stress because the material has less time to generate dislocations and relax the high stresses involved. It can be seen that the sensitivity of the results with strain rate is relatively small, as already shown for a single void in fcc Cu [17].

At strain rates much lower than the ones studied here, thermally activated processes will compete with the processes described in this work, including thermally activated climb and cross-slip, possibly leading to different final microstructures. Due to the limitations of MD it is difficult to reach lower strain rates and compare to constitutive models which include strain-rate dependence like the Hoge–Mukherjee (HM) [59], Steinberg–Lund [60] and Preston–Tonks–Wallace (PTW) [61] models. One way to test some aspects of these models would be to run our simulations at different temperatures, but this is beyond the scope of the present paper.

The dislocation density for Au never decreases during loading in our simulations (Fig. 10). For Ta, instead, MD simulations show a decrease in the dislocation density [29]. Such a decrease occurs because screw dislocations in bcc metals have compact cores that can cross-slip easily and react with other screw dislocations in order to annihilate. In fcc metals, on the contrary, even full dislocations still have extended cores (stacking fault bound by two partials) and the cross-slip of a screw dislocation needs an additional activation energy. Thus, accumulation of partial dislocations will continue until saturation.

The von Mises stress σ_{VM} in the hardening regime features two different power law dependencies as a function of dislocation density ρ_d (Fig. 11). In the initial stages of
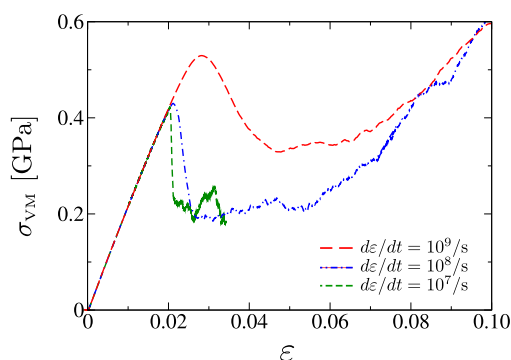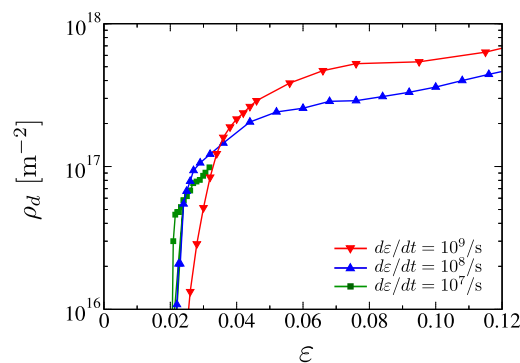

Fig. 10. Dislocation density ρ_d as a function of strain ε for strain rates of $d\varepsilon/dt = 10^7, 10^8, 10^9$ s^{-1}.
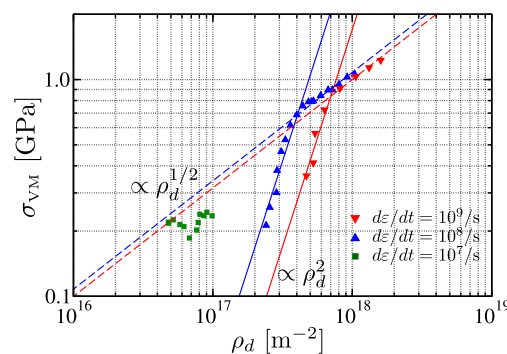

Fig. 11. The von Mises stress as a function of dislocation density ρ_d for different strain rates. For the cases of $d\varepsilon/dt = 10^8$ and 10^9 s^{-1}, a power law of ρ_d^2 is calculated at the onset of plastic deformation, but it changes to Taylor hardening $\rho_d^{1/2}$ once the dislocation forest develops.

plastic deformation, the power law is $\sigma_{VM} \propto \rho_d^2$, but later becomes $\sigma_{VM} \propto \rho_d^{1/2}$ as in the classic Taylor hardening [62] regime. However, the prefactor in the resulting Taylor hardening regime is slightly different. The often-used prefactor is given by $\alpha Gb \sim 4$ Pa m, where α is a material-dependent factor ($\alpha \sim 0.5$) and G is the shear modulus, while our simulations yield a pre-factor of 1.5 Pa m. We note that, in the initial stages of plasticity, Taylor hardening is not expected, given that there is not a well-developed dislocation forest. However, Fig. 5 shows a dense forest already present at a 3% strain.

4.6. Connection to experiments

Kiritani and coworkers [63] have studied experimentally the deformation of Au at high strain rates, up to 10^6 s^{-1}, and found dislocation densities of $\sim 2 \times 10^{14}$ m^{-2} in recovered samples. We are not aware of any other experimental work in Au analyzing dislocation densities at higher strain rates like the ones used here. Dynamic X-ray diffraction can provide a way to measure how fast the plastic relaxation is and to estimate dislocation densities during loading [13]. Dislocation densities are expected to increase with strain rate, and the density in recovered samples of fcc metals is expected to decrease by a factor of 10–10^3 compared

Fig. 9. Stress–strain curves for strain rates of $d\varepsilon/dt = 10^7, 10^8, 10^9$ s^{-1}.
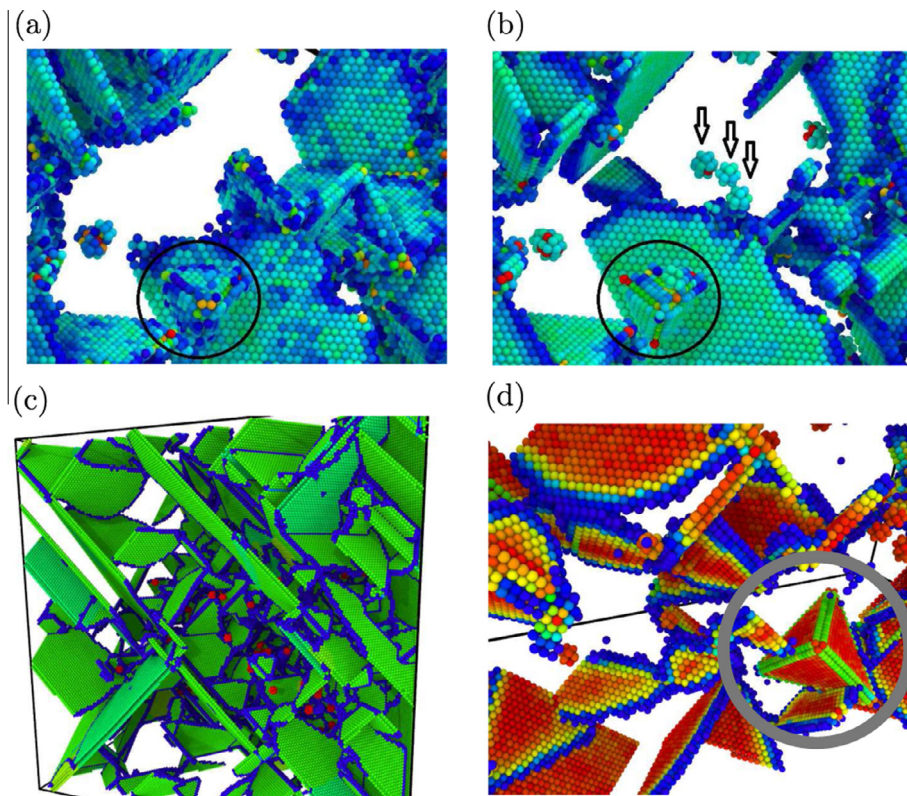
Fig. 12. (a) Pre-annealing and (b) post-annealing snapshots showing vacancy formation. Here, what seems to be the retraction of a partial dislocation leads to the formation of three vacancies, indicated with arrows. This mechanism is repeated throughout the sample. Non-hollow stacking fault tetrahedra (SFTs) survive the annealing process. (c) Vacancies (red dots) resulting from dislocation motion and reactions, which are present at the end of the relaxation of our sample, will likely lead to the formation of SFTs, as observed experimentally in Au samples recovered after high-strain-rate deformation [63]. (d) Intersection of SFs leads to a SFT. However, inside the SFT there are perfect fcc atoms, without vacancies, unlike what is usually observed in radiation damage, where there is a vacancy cluster in the core of the SFT [66,67]. Color is proportional to the centrosymmetry parameter with different color scales to emphasize certain defects. (For interpretation of the references to colour in this figure legend, the reader is referred to the web version of this article.)

with the density during loading [64]. Since we obtain densities of $\sim 10^{17}\,\mathrm{m}^{-2}$ during loading at $10^8\,\mathrm{s}^{-1}$, a value of $\sim 10^{14}\,\mathrm{m}^{-2}$ could be expected in recovered samples at lower strain-rate loading.

Tawara et al. [63] also suggested that dislocation-free plasticity and the generation of large number of vacancy clusters might play a role in the deformation of Au at high strain rates. In our simulations of single-crystal Au under compression we do not observe any of those effects. On the contrary, dislocation plasticity plays the main role in the deformation of Au.

In order to roughly mimic long-term thermal recovery, both thermal cycling and a zero-pressure barostat were applied to the sample after unloading. The sample was heated with a temperature ramp lasting 10 ps, until it reached 700 K. It was kept at high temperature, well below the melting temperature, for 10 ps, and then the temperature was ramped down to 10 K over 10 ps. This final configuration was analyzed to identify the recovered microstructure shown in Fig. 12. We observe a large decrease in full and partial dislocation densities, together with nearly one order of magnitude decrease in the SF density. This decrease is accompanied by the formation of

multiple vacancies and vacancy clusters, as shown in Fig. 12(a) and (b) (from 51 individual vacancies prior to recovery to 251 after recovery). These vacancies will likely diffuse and join at long time scales, leading to SF tetrahedra (SFTs) [65], as observed by Tawara et al. [63] (see Fig. 12(c) and (d)). Therefore, we propose that the immense concentration of SFTs observed experimentally in recovered samples is likely a result of the fast unloading and not of dislocation-free plasticity during loading. Future multiscale studies including vacancy cluster diffusion might be able to shed light into this issue.

5. Conclusions

We performed MD simulations of nanoporous gold under high strain rates, similar to those achieved with explosives and high-power lasers (the results should be similar for other fcc materials with low stacking fault energy). The mechanical behavior of the nanofoam is significantly different from the behavior of materials with macroscopic porosity, where plastic yielding is typically assumed to be independent of pore size [15]. At the onset of plastic deformation, we found a behavior in which pores behave as if

they were isolated from each other. At higher deformations, due to the close proximity between pores, dislocations from different sources start to interact.

The values of yield stress from the simulations were found to be comparable to the ones found in the literature for gold nanofoams [68] using nanoindentation. The flow stress increased with strain rate within the range 0.4–0.7 GPa. The shear stress in the hardening regime has a power-law dependence with dislocation density: in the initial stages of plastic deformation the power is 2, and for higher densities the power is 0.5, as in the Taylor hardening regime.

The velocity of the dislocations was found to be elevated (60% of the speed of sound), but is reduced dramatically due to dislocation interactions once the dislocation forest develops. Dislocation densities during loading might be accessible to experiments, and we calculated the total dislocation densities without distinguishing mobile dislocations from sessile dislocations. Total densities ($\sim 10^{17}$ m^{-2}) were significantly higher than densities found in recovered samples. This is not unexpected, and it has been already discussed for shock-loading simulations [64]. We also proposed a simple estimate of mobile dislocation densities, and found them to be one order of magnitude lower than the total dislocation density. During the unloading process, the dislocation and stacking fault densities were reduced notably, leaving behind a large number of vacancy clusters. The vacancy clusters can form larger clusters which can collapse into SFTs, as observed by Kiritani and co-workers [63].

The lack of length scales in the current formulation of most continuum models dealing with porosity [15,16] renders the validity of such models questionable for their application to nanostructured materials. This study raises two issues which might be useful for the continuum scale community: (a) the often-used Taylor hardening, used for instance in the modified Gurson model [16], might not be valid for dislocation hardening originating from nanoscale porosity; and (b) the application of scale-free continuum models for nanostructured materials [15,16] is of doubtful validity and should be contrasted with results obtained from atomistic simulations and experiments. In particular, atomistic simulations provide unique insights in the understanding of plastic deformation of nanoporous materials, shedding light on phenomena such as nano-enhanced strength and ductility. Future constitutive models with porosity have to include not only a density-dependent yielding, but yielding which depends on pore size, pore distribution and strain rate.

Acknowledgments

References

[1] Meyers M, Mishra A, Benson D. Prog Mater Sci 2006;51:427.
[2] Bringa EM, Caro A, Wang Y, Victoria M, McNaney JM, Remington BA, et al. Science 2005;309:1838.
[3] Samaras M, Derlet PM, Van Swygenhoven H, Victoria M. Phys Rev Lett 2002;88:125505.
[4] Lu L, Shen Y, Chen X, Qian L, Lu K. Science 2004;304:422.
[5] Biener J, Hodge AM, Hayes JR, Volkert CA, Zepeda-Ruiz LA, Hamza AV, et al. Nano Lett 2006;6:2379.
[6] Sayle TXT, Ngoepe PE, Sayle DC. ACS Nano 2009;3:3308.
[7] Bringa EM, Monk JD, Caro A, Misra A, Zepeda-Ruiz L, Duchaineau M, et al. Nano Lett 2012;12:3351.
[8] Lee D, Wei X, Chen X, Zhao M, Jun S, Hone J, et al. Scr Mater 2007;56:437.
[9] Weissmüller J, Newman RC, Jin HJ, Hodge AM, Kysar JW. MRS Bull 2009;34:577.
[10] Reisman DB, Wolfer WG, Elsholz A, Furnish MD. J Appl Phys 2003;93:8952.
[11] Erhart P, Bringa EM, Kumar M, Albe K. Phys Rev B 2005;72:052104.
[12] Edwards J, Lorenz KT, Remington BA, Pollaine S, Colvin J, Braun D, et al. Phys Rev Lett 2004;92:075002.
[13] Bringa EM, Rosolankova K, Rudd RE, Remington BA, Wark JS, Duchaineau M, et al. Nat Mater 2006;5:805.
[14] Jarmakani H, Bringa E, Erhart P, Remington B, Wang Y, Vo N, et al. Acta Mater 2008;56:5584.
[15] Gurson AL. J Eng Mater Tech 1977;99:2.
[16] Wen J, Huang Y, Hwang K, Liu C, Li M. Int J Plasticity 2005;21:381.
[17] Traiviratana S, Bringa EM, Benson DJ, Meyers MA. Acta Mater 2008;56:3874.
[18] Bhatia M, Solanki K, Moitra A, Tschopp M. Metall Mater Trans A 2013;44:617.
[19] Tang Y, Bringa EM, Meyers MA. Acta Mater 2012;60:4856.
[20] Crowson DA, Farkas D, Corcoran SG. Scr Mater 2007;56:919.
[21] Crowson DA, Farkas D, Corcoran SG. Scr Mater 2009;61:497.
[22] Gyulassy A, Duchaineau M, Natarajan V, Pascucci V, Bringa EM, Higginbotham A, et al. IEEE Trans Visual Comput Graphics 2007;13:1432.
[23] Kolluri K, Demkowicz MJ. Acta Mater 2011;59:7645.
[24] Farkas D, Caro A, Bringa E, Crowson D. Acta Mater 2013;61:3249.
[25] Chen YC, Lu Z, Nomura Ki, Wang W, Kalia RK, Nakano A, et al. Phys Rev Lett 2007;99:155506.
[26] Nguyen LD, Warner DH. Phys Rev Lett 2012;108:035501.
[27] Seppälä ET, Belak J, Rudd RE. Phys Rev Lett 2004;93:245503.
[28] Bringa EM, Traiviratana S, Meyers MA. Acta Mater 2010;58:4458.
[29] Ruestes C, Bringa E, Stukowski A, Rodriguez-Nieva J, Bertolino G, Tang Y, Meyers M. Scr Mater 2013;68:817.
[30] Kimminau G, Erhart P, Bringa EM, Remington B, Wark JS. Phys Rev B 2010;81:092102.
[31] Lubarda V, Schneider M, Kalantar D, Remington B, Meyers M. Acta Mater 2004;52:1397.
[32] Davila LP, Erhart P, Bringa EM, Meyers MA, Lubarda VA, Schneider MS, et al. Appl Phys Lett 2005;86:161902.
[33] Marian J, Knap J, Campbell G. Acta Mater 2008;56:2389.
[34] Weinberger CR, Cai W. J Mater Chem 2012;22:3277.
[35] Zepeda-Ruiz LA, Sadigh B, Biener J, Hodge AM, Hamza AV. Appl Phys Lett 2007;91:101907.
[36] Daw MS, Baskes MI. Phys Rev B 1984;29:6443.
[37] Foiles SM, Baskes MI, Daw MS. Phys Rev B 1986;33:7983.
[38] Crowhurst JC, Armstrong MR, Knight KB, Zaug JM, Behymer EM. Phys Rev Lett 2011;107:144302.
[39] Biener J, Hodge AM, Hamza AV. Appl Phys Lett 2005;87:121908.
[40] Wu L, Markenscoff X. J Elast 1996;44:131.
[41] Kelchner CL, Plimpton SJ, Hamilton JC. Phys Rev B 1998;58:11085.
[42] Shehadeh MA, Bringa EM, Zbib HM, McNaney JM, Remington BA. Appl Phys Lett 2006;89:171918.

[43] Germann T, Holian B, Lomdahl P, Tanguy D, Mareschal M, Ravelo R. Metall Mater Trans A 2004;35:2609.
[44] Bulatov VV, Wolfer WG, Kumar M. Scr Mater 2010;63:144.
[45] Bringa E, Lubarda V, Meyers M. Scr Mater 2010;63:148.
[46] Stukowski A, Albe K. Model Simul Mater Sci Eng 2010;18:085001.
[47] Marian J, Knap J, Ortiz M. Phys Rev Lett 2004;93:165503.
[48] Grace F, Inman M. Metallography 1970;3:89.
[49] Murr L. Thin Solid Films 1969;4:389.
[50] Mordehai D, Kelson I, Makov G. Phys Rev B 2006;74:184115.
[51] Tsuzuki H, Branicio PS, Rino JP. Appl Phys Lett 2008;92:191909.
[52] Olmsted DL, Jr LGH, Curtin WA, Clifton RJ. Model Simul Mater Sci Eng 2005;13:371.
[53] Bitzek E, Gumbsch P. Mater Sci Eng: A 2004;387-389:11.
[54] Bitzek E, Gumbsch P. Mater Sci Eng: A 2005;400-401:40.
[55] Hatano T. Phys Rev Lett 2004;93:085501.
[56] Orowan E. Proc Phys Soc 1940;52:8.
[57] Higginbotham A, Bringa EM, Marian J, Park N, Suggit M, Wark JS. J Appl Phys 2011;109:063530.
[58] Quinney H, Taylor G. Proc R Soc London 1937;163:157.
[59] Hoge K, Mukherjee A. J Mater Sci 1977;12:1666.
[60] Steinberg DJ, Lund CM. J Appl Phys 1989;65:1528.
[61] Preston DL, Tonks DL, Wallace DC. J Appl Phys 2003;93:211.
[62] Meyers MA, Chawla KK. Mechanical behavior of materials. Englewood Cliffs, NJ: Prentice-Hall; 1998.
[63] Tawara T, Matsukawa Y, Kiritani M. Mater Sci Eng: A 2003;350:70.
[64] Cao B, Bringa EM, Meyers MA. Metall Mater Trans A 2007;38:2681.
[65] Uberuaga BP, Hoagland RG, Voter AF, Valone SM. Phys Rev Lett 2007;99:135501.
[66] Wirth B, Bulatov V, de la Rubia TD. J Nucl Mater 2000;283-287:773.
[67] Osetsky Y, Bacon D. Nucl Instrum Methods B 2001;180:85.
[68] Biener J, Hodge AM, Hamza AV, Hsiung LM, Joe H Satcher J. J Appl Phys 2005;97:024301.